ADVANCED MATERIALS

Supporting Information

Unveiling Strong Ion–Electron–Lattice Coupling and Electronic Antidoping in Hydrogenated Perovskite Nickelate

Lei Gao, Huimin Wang, Fanqi Meng, Huining Peng, Xiangyu Lyu, Mingtong Zhu, Yuqian Wang, Chao Lu, Jin Liu, Ting Lin, Ailing Ji, Qinghua Zhang*, Lin Gu, Pu Yu, Sheng Meng*, Zexian Cao and Nianpeng Lu*

Supporting Information

Unveiling Strong Ion–Electron–Lattice Coupling and Electronic Antidoping in Hydrogenated Perovskite Nickelate

Lei Gao, Huimin Wang, Fanqi Meng, Huining Peng, Xiangyu Lyu, Mingtong Zhu, Yuqian Wang, Chao Lu, Jin Liu, Ting Lin, Ailing Ji, Qinghua Zhang*, Lin Gu, Pu Yu, Sheng Meng*, Zexian Cao and Nianpeng Lu*

*Corresponding authors.
Emails: zqh@iphy.ac.cn, smeng@iphy.ac.cn and lunianpeng@iphy.ac.cn

This file includes:

Figures S1-S12 refer to the electric-field controlled reversible hydrogen ion intercalation and formation of a new robust H-NNO phase.

Figure S1. Reciprocal space mappings (RSM) of the pristine NNO and gated H-NNO.

Figure S2. Electric-field controlled reversible phase transformation between NNO and H-NNO.

Supplementary Note 1. Identification of the gating mechansim through isotrope calibration (**Figures S3** and **S4**).

Figure S3. Deuterium (D) isotope calibration in ionic liquid gating.

Figure S4. ^{18}O isotope calibration.

Supplementary Note 2. Threshold electric voltage for ionic liquid gating induced phase transformation (**Figure S5**).

Figure S5. Identification of gating threshold electric voltage.

Figure S6. Comparison between the obtained phase through ionic liquid gating and noble Pt thermal catalysis in forming gas of Ar and H_2 (5%).

Figure S7. Stability test of the newly formed phase with time.

Figure S8. Thickness dependent phase transformation.

Figure S9. Thermal stability of the H-NNO.

Figure S10. Strain dependent phase transformation on different substrates.

Figure S11. Phase transformation from NNO to H-NNO on STO substrate.

Figure S12. Expansion or extraction of various materials with ion (H^+, O^{2-} and Li^+) intercalation.

Figures S13-S20 are concerned with lattice modification with hydrogen ion intercalation from STEM and theoretical calculations.

Figure S13. STEM image and EELS mappings for NNO phase.

Figure S14. Structural domains ($[110]_o$ and $[001]_o$ or 0° and 90°) of orthorhombic NNO grown on pesudocubic LAO (001) substrate.

Figure S15. Low magnification STEM images of NNO and H-NNO phases.

Figure S16. STEM images and lattice profiles of NNO and H-NNO phase.

Supplementary Note 3. Comparison between XAS and EELS measurements (**Figures 3c**, **3d** and **Figure S17**)

Figure S17. EELS of the Ni L-edge and O K-edge.

Figure S18. Calculated lattice structure of $H_{0.25}NNO$.

Figure S19. Calculated lattice structures of pristine NNO and hydrogen ion intercalated H-NNO with the oxygen octahedral rotation pattern of $--+$(Glazer notation).

Figure S20. Calculated hydrogen concentration dependent Ni-O-Ni band angle (θ), lattice expansion (ΔV) and Coulomb repulsion (U).

Figures S21-S25 illustrate the electronic structure variation with hydrogen ion intercalation.

Figure S21. Comparison of X-ray absorption spcetra of Ni L-edge and O K-edge for the H-NNO on different substrates.

Figure S22. Phase transformation with corresponding X-ray absorption spectra for $SmNiO_3$, which show similar results to that of $NdNiO_3$.

Figure S23. Comparison of Ni L-edge and O K-edge X-ray absorption spectra among NNO, H-NNO and NiO.

Figure S24. Projected density of states (PDOS) of the pure electron doped NNO (e-NNO).

Figure S25. Projected density of states (PDOS) of the distortive NNO.

Figure S26 shows the electric-field controlled hydrogen ion intercalation to fabricate the selective micropatterns.

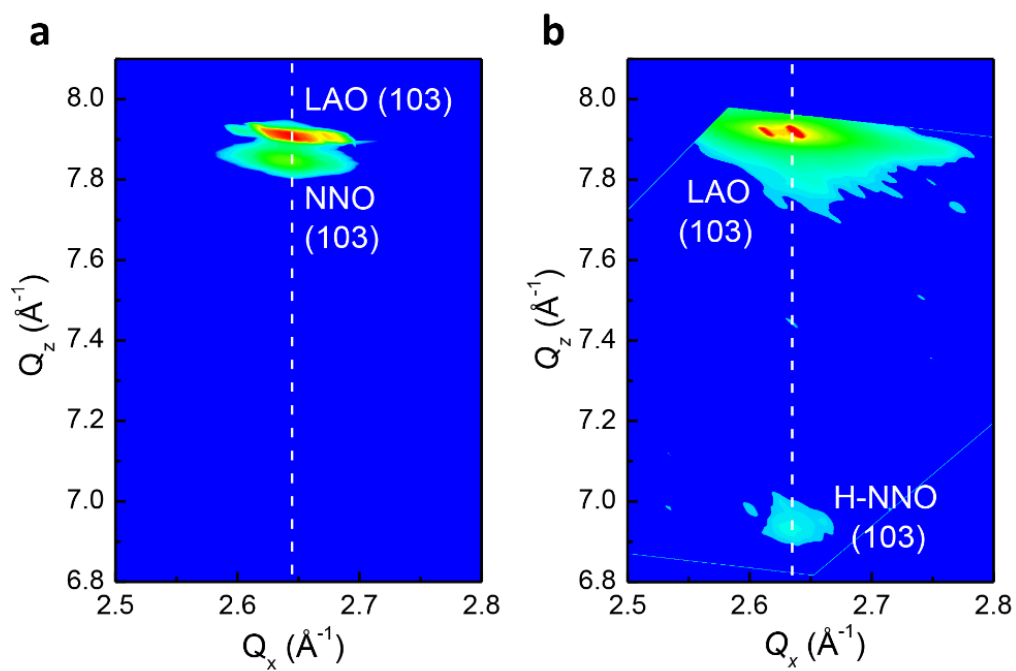**Figure S26.** Fabrication process of the selective micropattern through ionic liquid gating.

Figure S1. Reciprocal space mappings (RSM) of the (a) NNO and (b) H-NNO, indicating that the in-plane lattices of both as-grown NNO and obtained H-NNO are coherent on the substrate.
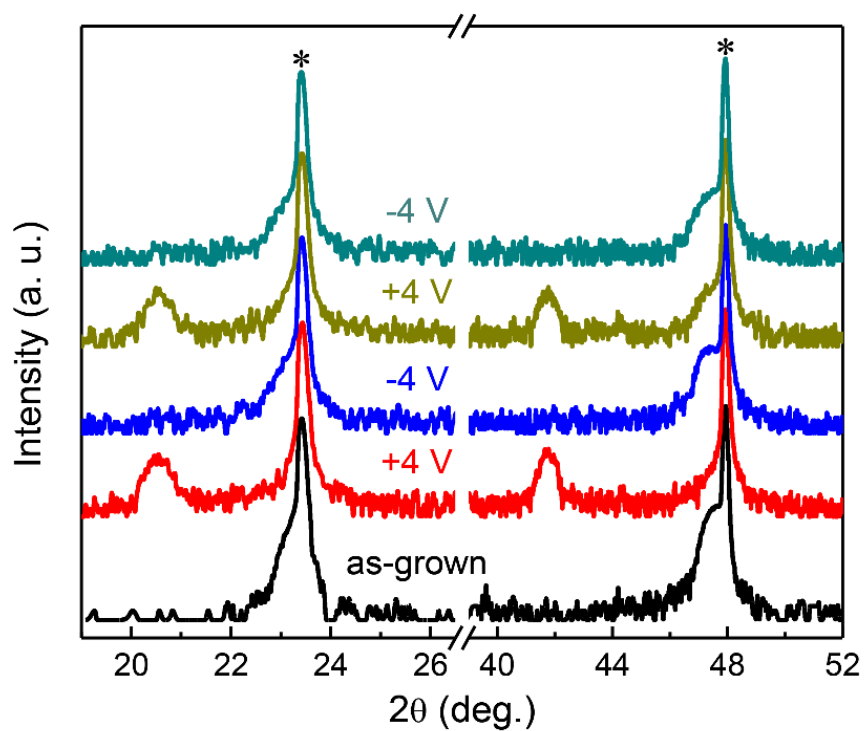
Figure S2. Reversible phase transformation between NNO and H-NNO with a gating voltage of +4 V and -4 V, respectively. The asterisks indicate the substrate diffraction peaks.

Supplementary Note 1. Identification of the gating mechansim through deuterium and ^{18}O isotrope calibration (Figures S3 and S4).

To provide solid evidence about the origin of the hydrogen ion in the H-NNO phase, we labeled the ionic liquid with heavy water (D$_2$O), by dipping a tiny droplet of D$_2$O into the ionic liquids (DEME-TFSI). Then, the treated ionic liquids went through an ultrasonic agitation and were baked in the dry air oven with the temperature 110 °C for 2 hours. With this developed ionic liquids, we obtained successfully the same phase transformations, and we subsequently carried out the SIMS measurement. By the depth profile measurements, it is found that the deuterium ions are uniformly distributed inside the H(D)-NNO sample (**Figure S3a**), and SIMS spectra (**Figure S3b**) around m/Z ~ 2.0 also shows a clear signal from D ions.

Moreover, to further verify the dominated hydrogenation effect in the phase transformation, we used the isotope ^{18}O to label the ionic evolution by ^{18}O$_2$ gas. To measure the ^{18}O signal, the H-NNO thin film were first obtained through ionic liquid gating, and then thermally annealed in ^{18}O$_2$ gas at 90 °C for 2 hours. The SIMS results show that except a tiny of ^{18}O in the surface layer, negligible ^{18}O can be detected in the gated sample (**Figure S4**). Therefore, we can conclude that the ILG induced structural transformation is strongly associated with the hydrogenation process.
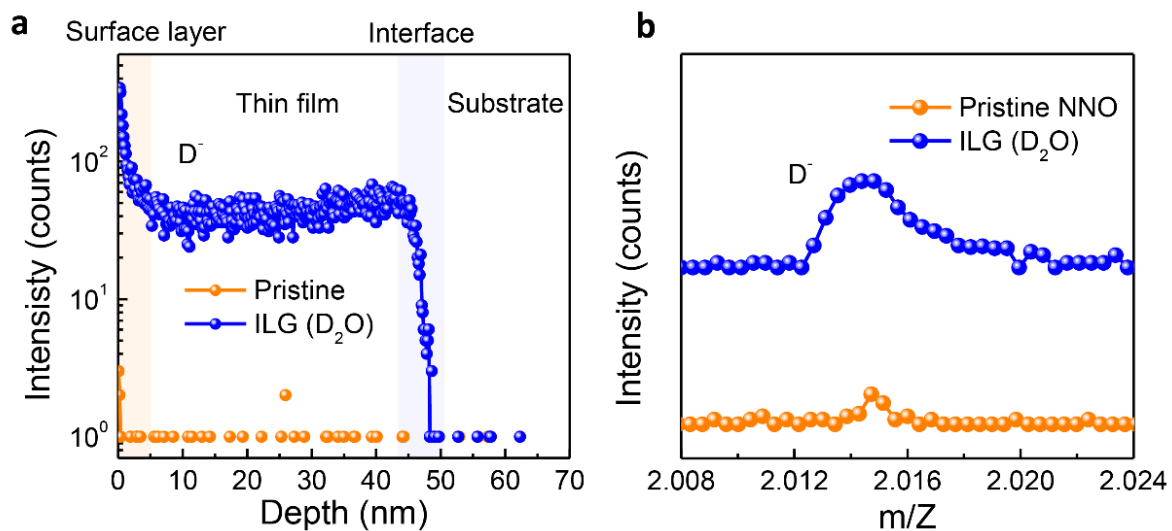
Figure S3. Deuterium isotrope calibration in ionic liquid gating. a) Depth profiles of the D⁻ ions in the pristine and gated NNO films with heavy water (D$_2$O) doped ionic liquid. b) Comparison of SIMS spectra around m/z ≈ 2.0 for pristine NNO and gated sample.
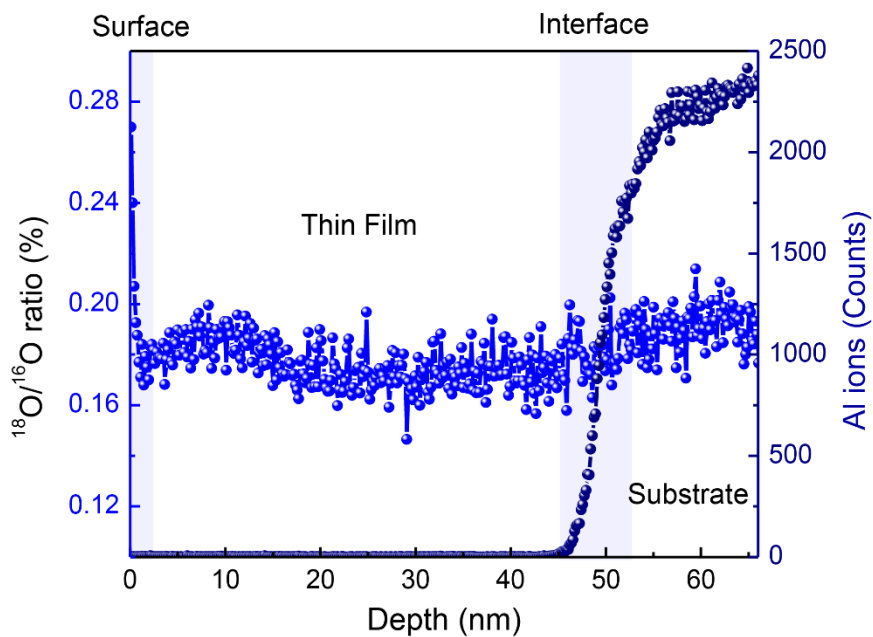
Figure S4. Depth profile of ^{18}O ions in the H-NNO after thermal annealing in $^{18}O_2$ at 90 $^{\circ}$C with duration of 2 hours, in which the Al element is used to mark the interface between the thin film and substrate.

Supplementary Note 2. Threshold electric voltage for ionic liquid gating induced phase transforamtion (Figure S5)

To obtain further insights into the relationship between bias voltage and structural change, we have performed the in-situ XRD measurement by increasing gating voltage, as summarized in **Figure S5a**. The curves were obtained with gating voltage interval of 0.2 V and dwelling time of 500 seconds at each voltage. The θ–2θ scans around $NdNiO_3$ (002) show that no obvious diffraction peak change was observed with V_G increasing up to ~1.0 V, while a further increase of V_G leads to a slight shift of the peak position to a lower angle. When the voltage reaches about 1.6 V, the intensity of the NNO phase peak decreases and the new phase peak gradually appears at the low angle position (~42°), which corresponds to the hydrogenation phase transformation process.

Notably, the hydrogenation structural transformation possesses a threshold gating voltage, and higher voltage corresponds to shorter transition time. In order to determine the threshold bias more precisely, we applied different bias voltages to the same sample for one hour each time to see the final structure change, as shown in **Figure S5b**. At 1.3 V bias, a new phase (~42°) gradually begin to appear, but at 1.2 V, there is no new phase peak. XRD results show that the threshold voltage is between 1.2 V and 1.3 V, which is consistent with the hydrogenation mechanism by water hydrolysis.
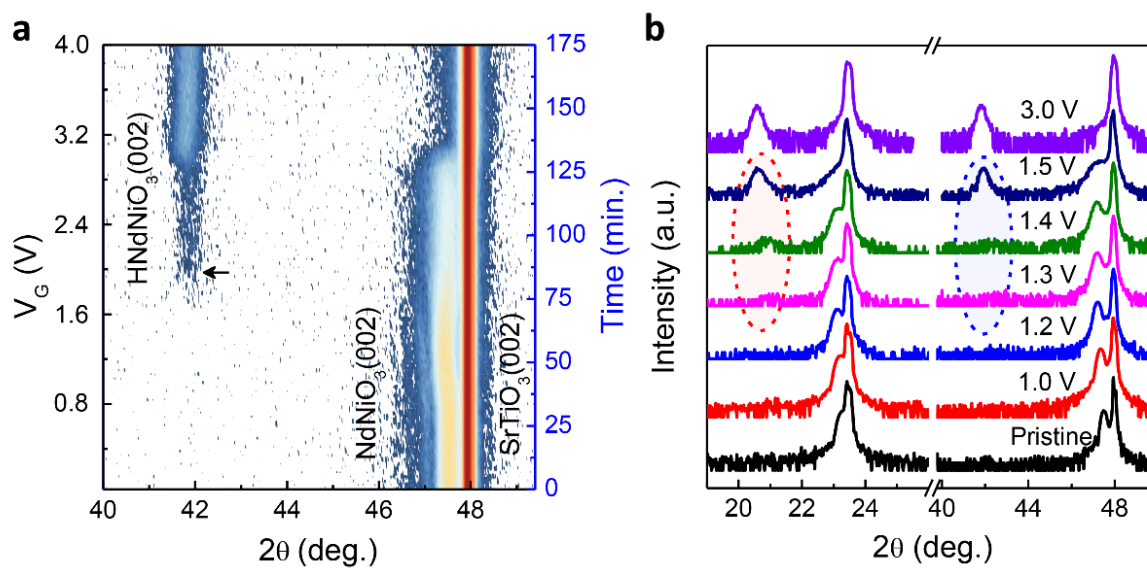
Figure S5. Identification of gating threshold electric voltage. a) In-situ XRD θ-2θ scans around the NdNiO₃ (002) peak as a function of increasing V_G. The curves were obtained with gating voltage interval of 0.2 V and dwelling time of 500 seconds at each voltage. b) Comparison of XRD θ–2θ scans for NdNiO₃ samples with different bias voltage gating for 1 hour, indicating the threshold bias is between 1.2 V and 1.3 V.
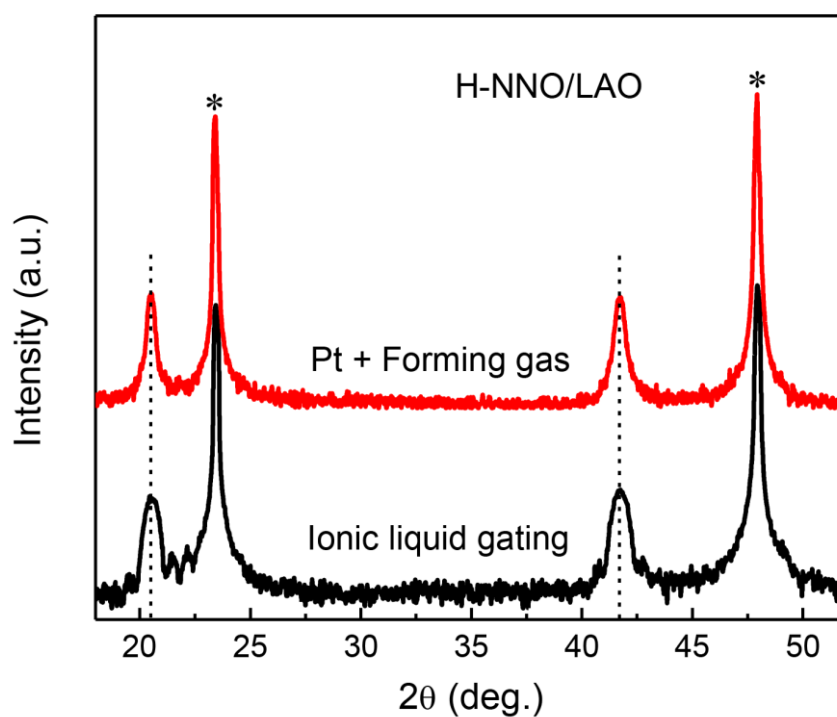
Figure S6. Comparison between the obtained new phase through the methods of ionic liquid gating and noble Pt thermal catalysis in forming gas (Ar:H_2 = 95:5). We can see that the nearly same final new phase with the lattice expansion of 13.2% can be obtained.
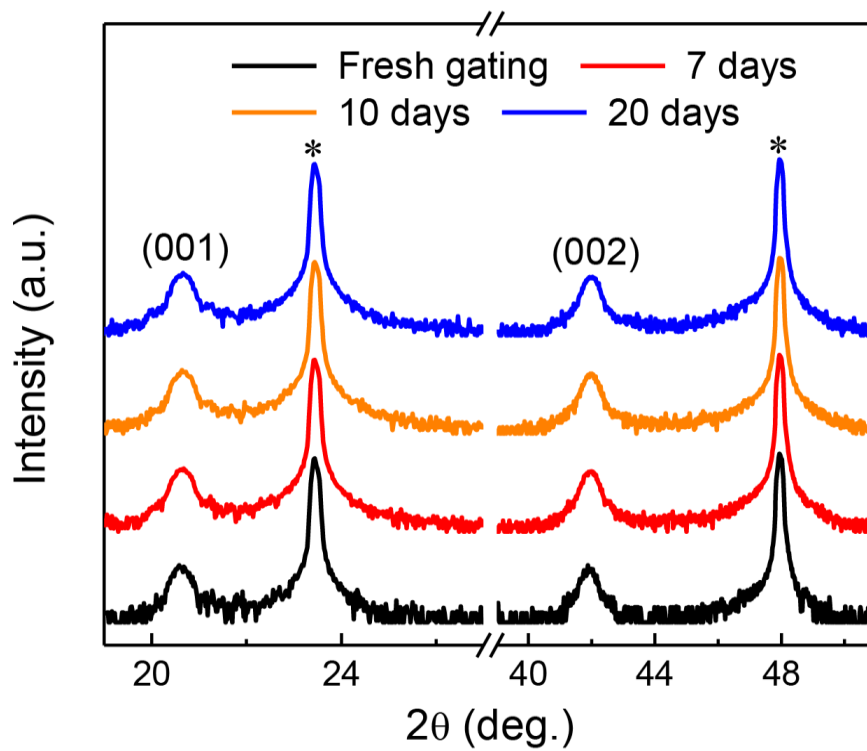
Figure S7. Stability test of the newly formed phase with time, from which we know that the new hydrogenated phase is very stable.
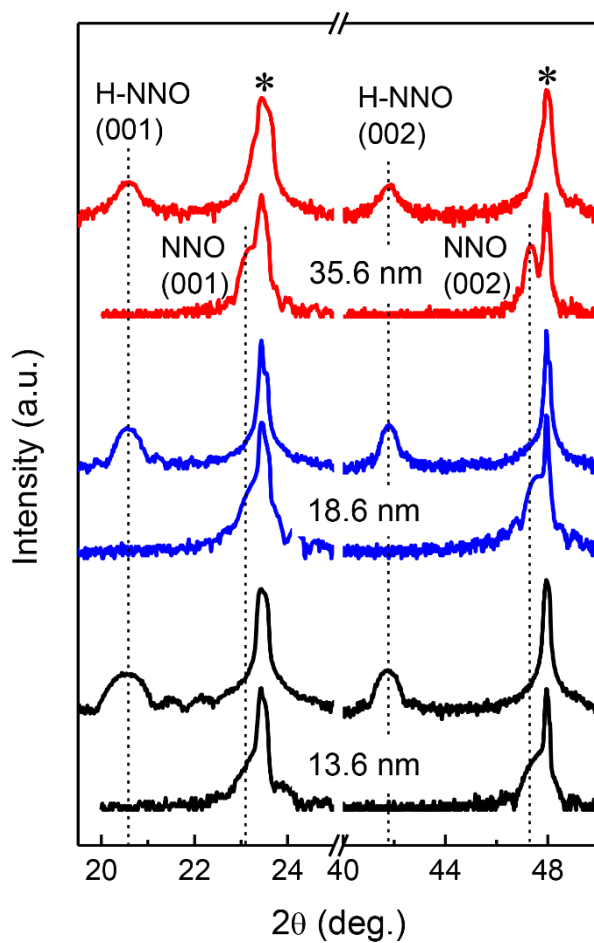
Figure S8. Thickness dependence of phase transformation with the NNO film thickness of 13.6 nm, 18.6 nm and 35.6 nm, respectively, which further show that the phase transformation is a bulk effect instead of an interficial effect.
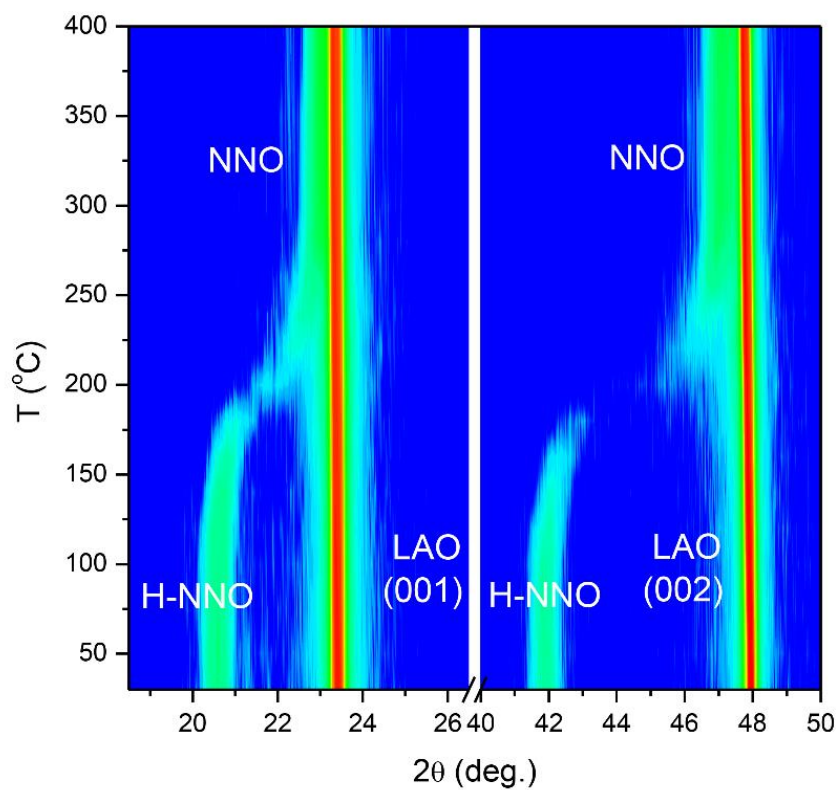
Figure S9. Thermal stability of the H-NNO. In the measurement, the temperature interval was set as 10 °C, and the sample was held at each temperature for 10 min in the atmosphere of air.
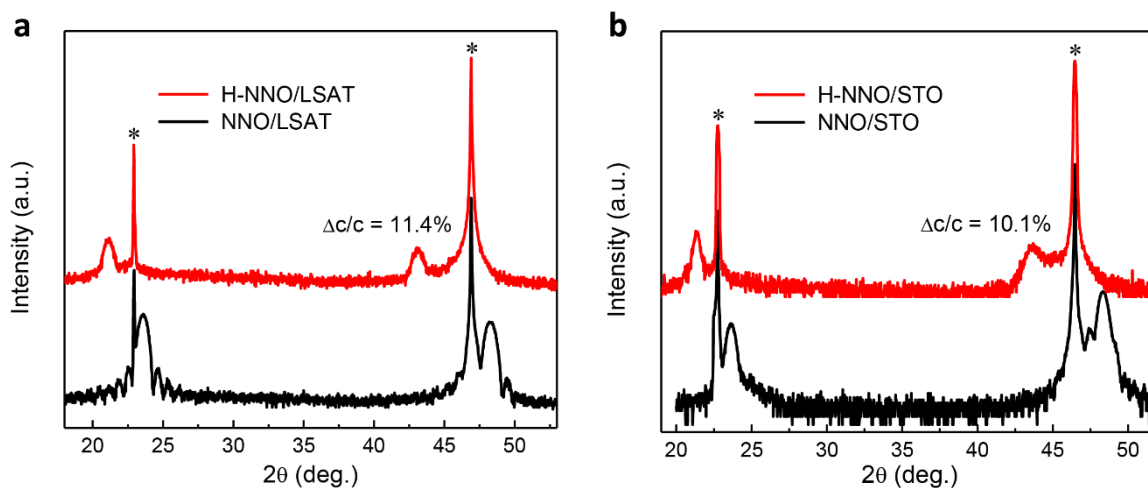
Figure S10. Strain-dependent phase transformation in samples grown on (a) LSAT(001) and (b) STO(001) substrates. The corresponding lattice expansion are 11.4% and 10.1%, respectively.
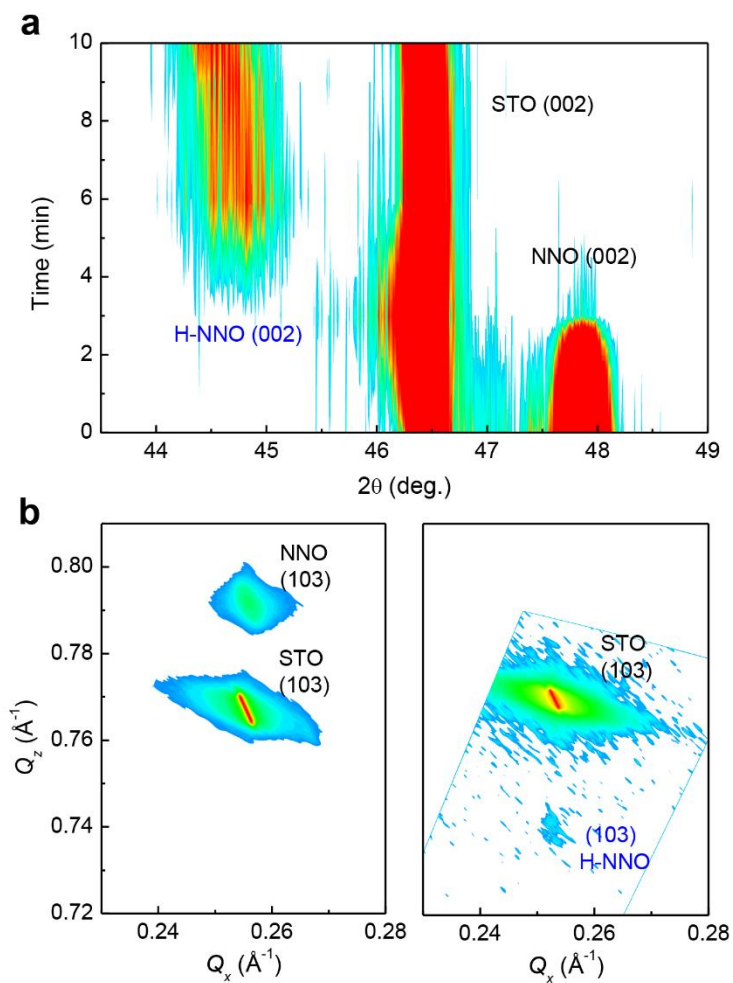
Figure S11. Electric-field controlled phase transformation from NNO to H-NNO on STO substrate. a) Phase transformation from NNO to H-NNO. b) RSM of the pristine NNO and H-NNO.
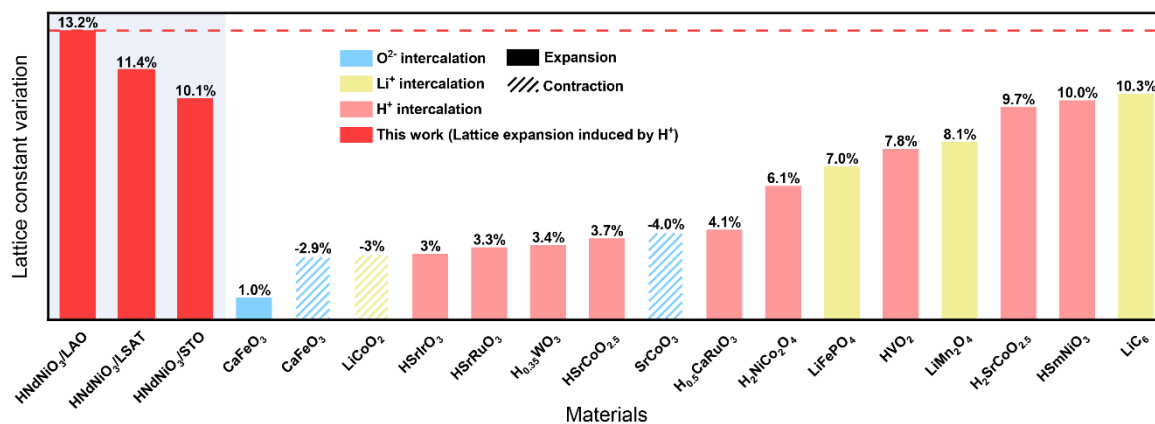
Figure S12. Lattice expansion or extraction of various materials with ion (H^+, O^{2-} and Li^+) intercalation [1-14]. The largest lattice expansion is manifested in H-NNO/LAO.
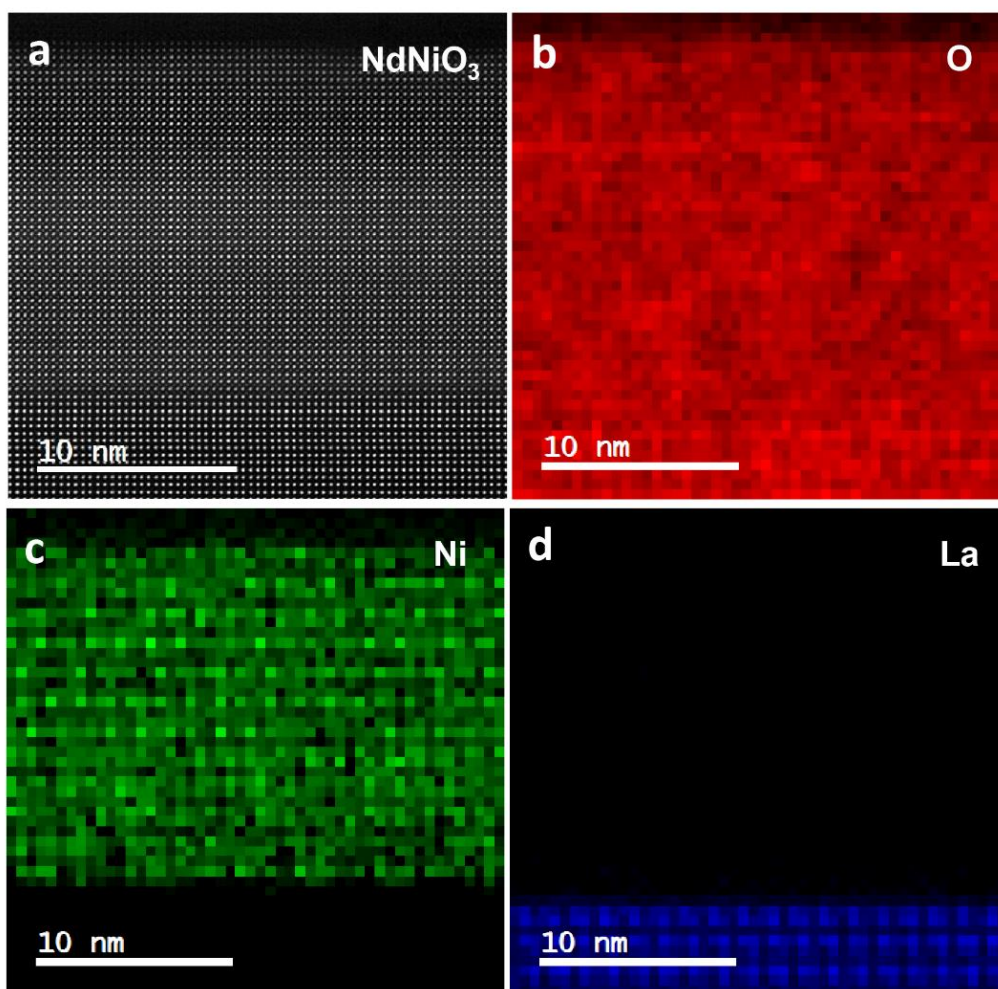
Figure S13. a) STEM image for NNO grown on LAO (001) substrate, and the EELS mappings referring to the element of (b) O, (c) Ni and (d) La. The latter two images indicate a sharp interface between the NNO thin film and LAO substrate.
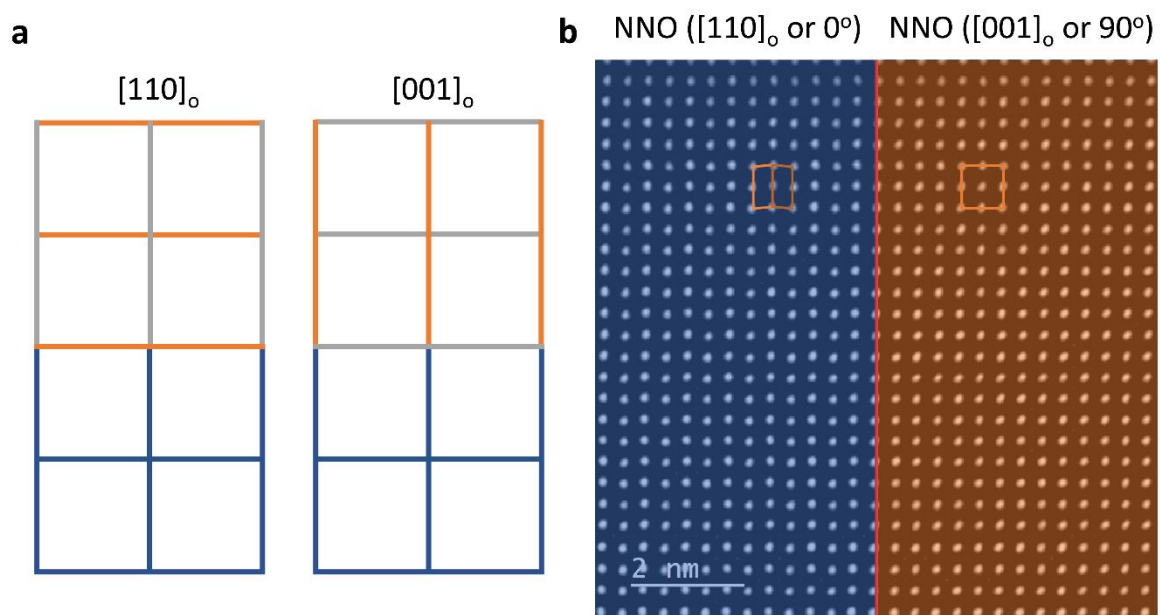
17

a

[110]$_o$ [001]$_o$

b   NNO ([110]$_o$ or 0°)   NNO ([001]$_o$ or 90°)

2 nm

Figure S14. a) NNO Thin film with orthorhombic lattice structure grown on pseudocubic LAO substrate which leads to the structure domains along [1 1 0]$_o$ and [0 0 1]$_o$ projections, respectively. b) Two structure domains along with [1 1 0]$_o$ and [0 0 1]$_o$ projections of NNO orthorhombic twinning correspond to 0° and 90° domain, respectively.
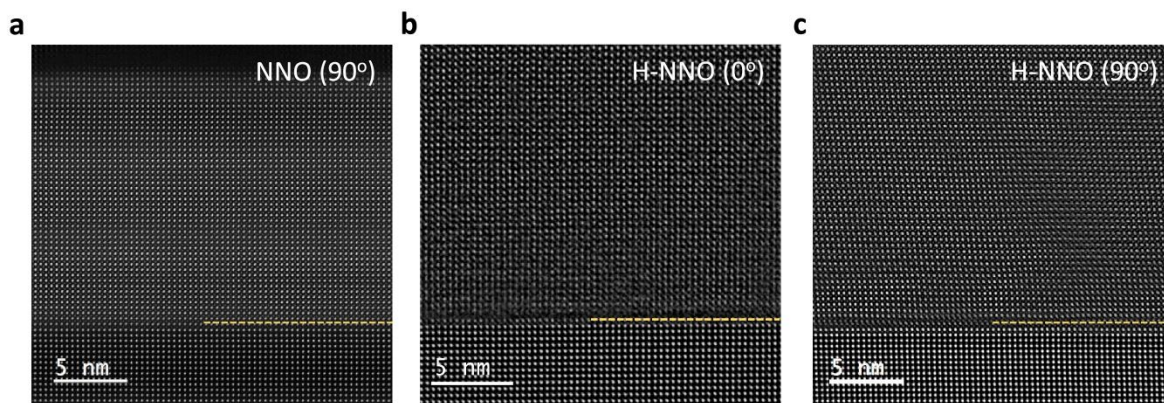
Figure S15. Low magnification STEM images of (a) NNO (90°) and H-NNO phases with (b) 0° and (c) 90° domain. We can see that for the pristine NNO phase, the interface is very shape, while for the obtained H-NNO phase a transitional interface can be clearly seen which may release the strain energy to accommodate the giant in-plane strain. Moreover, from the HAADF images of two domains, we can find that the lattice symmetry translates from orthorhombic to monoclinic structure.
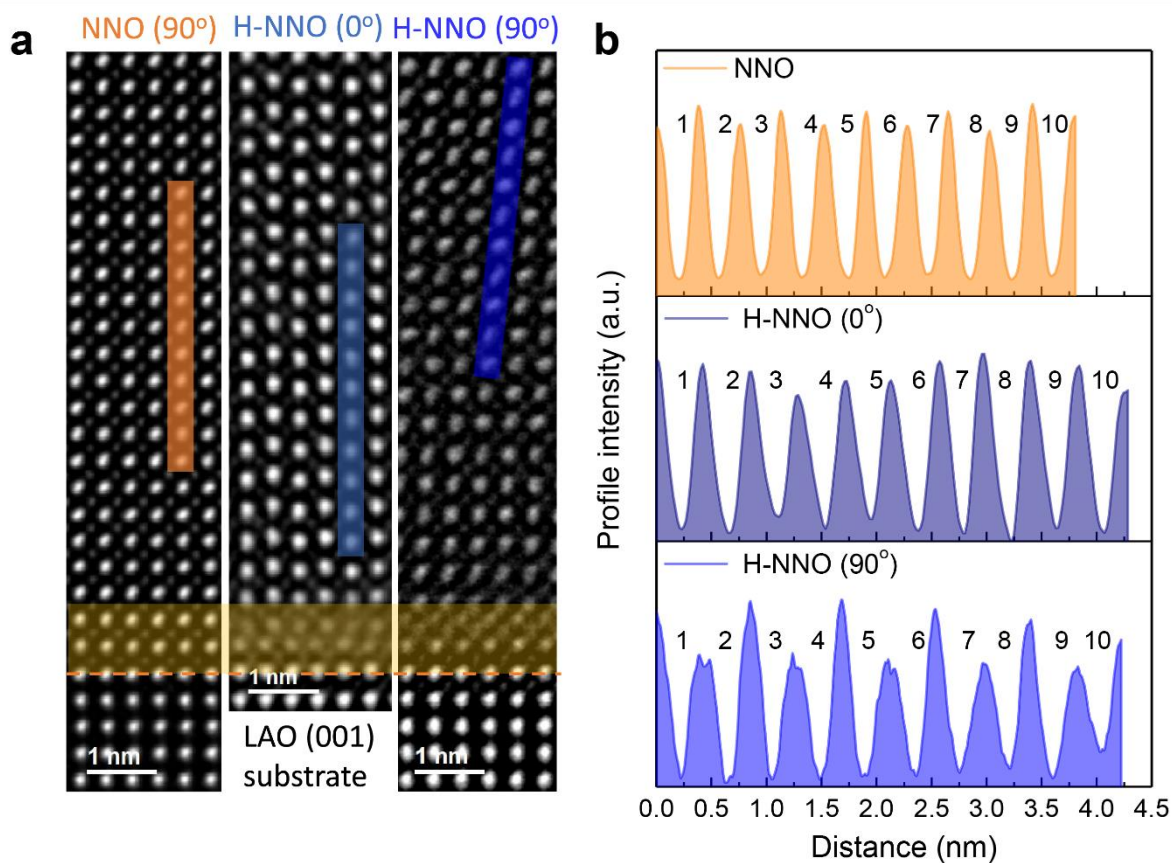
Figure 16. a) High magnification STEM images of NNO (90º), H-NNO (0º and 90º) domain, and (b) corresponding profiles marked in (a), from which we know that comparing with the pristine NNO, the lattice expansion is ~13% which is consistent with XRD measurement. Moreover, comparing with the pristine NNO phase in the HAADF images marked by the yellow shadow area, it can be found that there is a transitional buffer layer with 2-3 unit cells for the H-NNO phase which may be related to the broken oxygen octahedral connectivity at the interface due to the enhanced octahedral rotation.

Supplementary Note 3. Comparison between the XAS and EELS measurements (Figures 3c, 3d and Figure S17).

Both XAS and EELS correspond to the process of exciting core electrons to empty valence states allowed by the dipole selection rules [15, 16]. The main difference is that XAS is an optical dipole induced transition and EELS is an effective Coulomb transition. Both methods provide information about unoccupied density of states and electronic structure of materials, and correspondingly show similar results of spectra [17]. XAS typically shows a much better energy resolution than EELS to identify the change of spectral shape of the absorption edges. Compared with the average effect measured by XAS by using a millimeter-size X-ray spot, the advantage of EELS is its very high spatial resolution down to the nanometer level and the electron beam can be focused on a specific structure. As shown in **Figures 3c**, **3d** and **Figure S17**, XAS and EELS spectra show the very similar characteristics for both Ni *L*-edge and O *K*-edge.
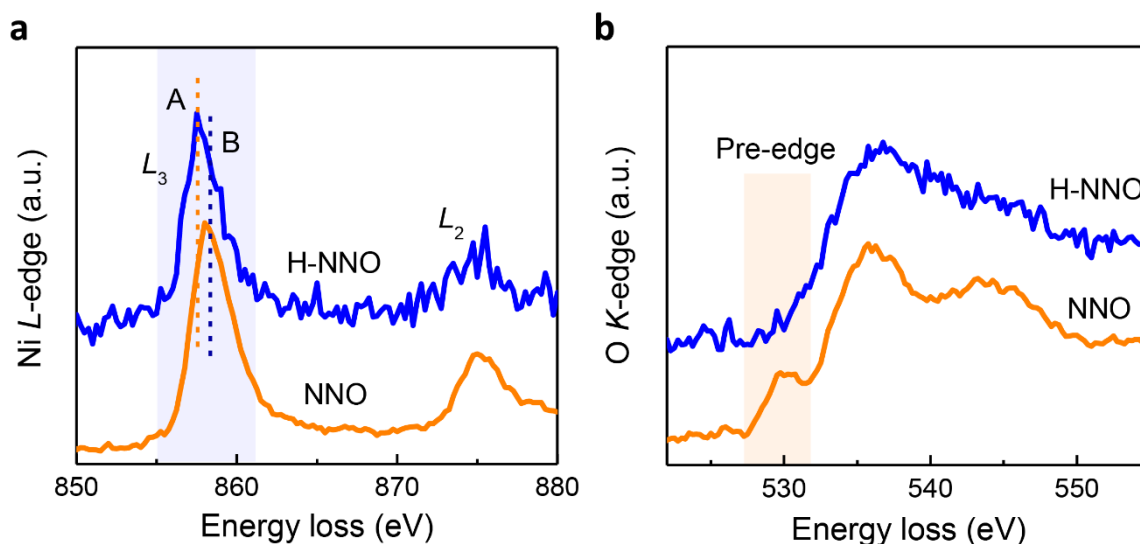
Figure S17. Electron energy loss spectra (EELS) of (a) Ni *L*-edge and (b) O *K*-edge, which show obvious change of nickel *L*-edge spectrum and the hybridization peaks in the oxygen *K*-edge. From the O *K*-edge, we see that there is a pre-peak around 530 eV for pristine NNO while it vanishes for H-NNO, indicating the unoccupied O 2*p* state hybridized with Ni 3*d* state near the Fermi level in NNO and occupied hybridized state in H-NNO. From the Ni *L*-edge, the peaks of the L_3 and L_2 have similar change with the X-ray absorption spectra in **Figure 3c**.
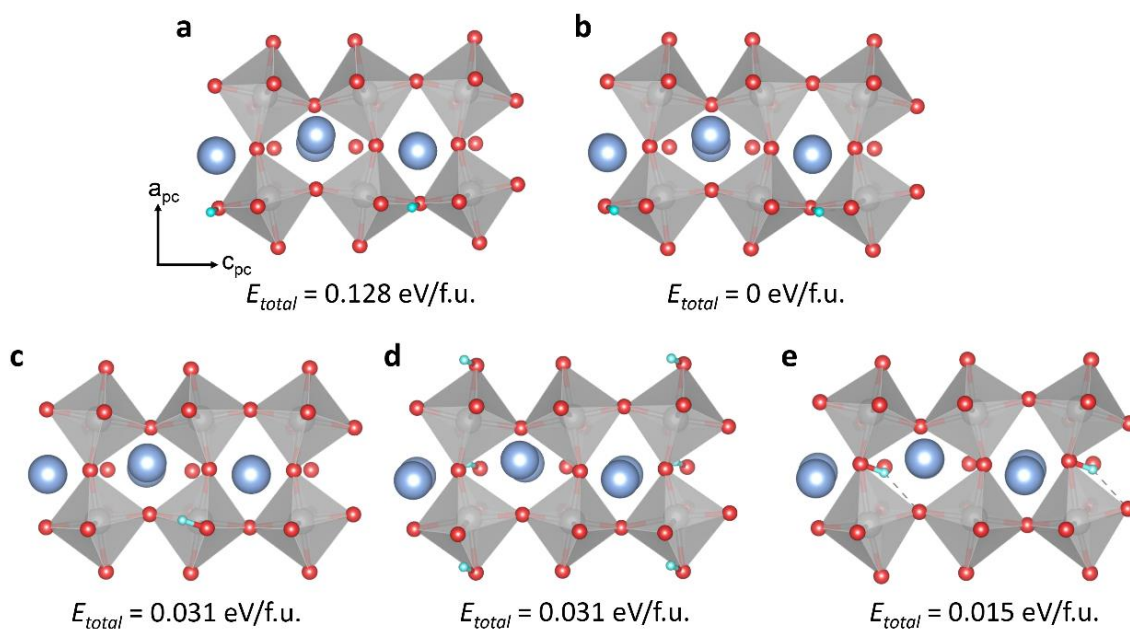
a

E_{total} = 0.128 eV/f.u.

b

E_{total} = 0 eV/f.u.

c

E_{total} = 0.031 eV/f.u.

d

E_{total} = 0.031 eV/f.u.

e

E_{total} = 0.015 eV/f.u.

Figure S18. Calculated lattice structure of $H_{0.25}$NNO. a-e) Possible lattice configurations of H-NNO with 0.25H/f.u.. The total energy is labeled, showing that lattice structure in panel (b) hosts the most stable hydrogen absorption position.
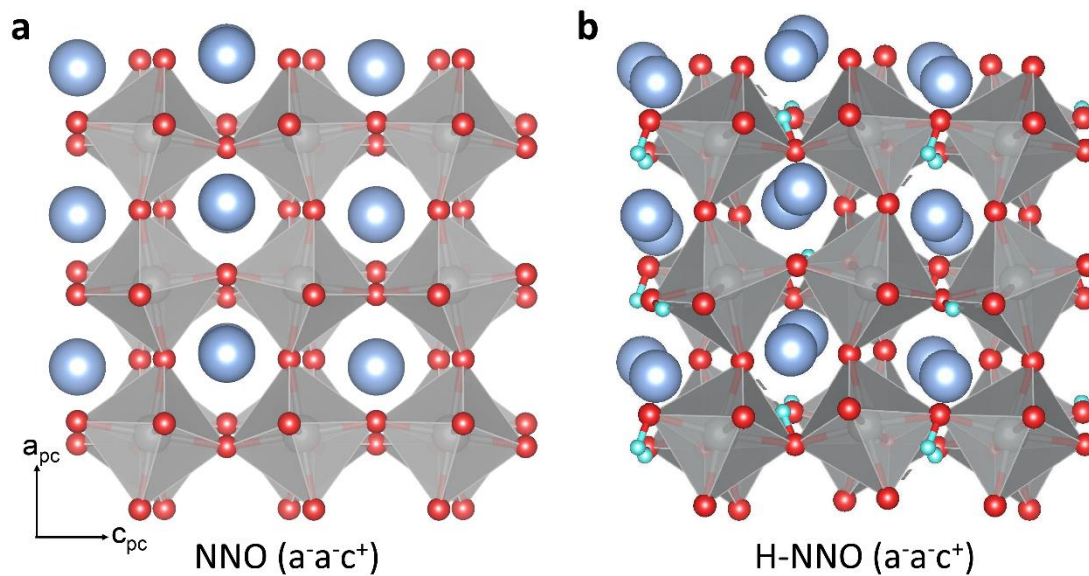
Figure S19. Lattice structures of (a) the pristine NNO and (b) H-NNO with [1 1 0]$_o$ projection (0° domain) (**Figure 2i** and **2k**), in which there is no change in the oxygen octahedral rotation pattern $^{--+}$ and the intercalation of hydrogen ion prompts the oxygen octahedral rotation.
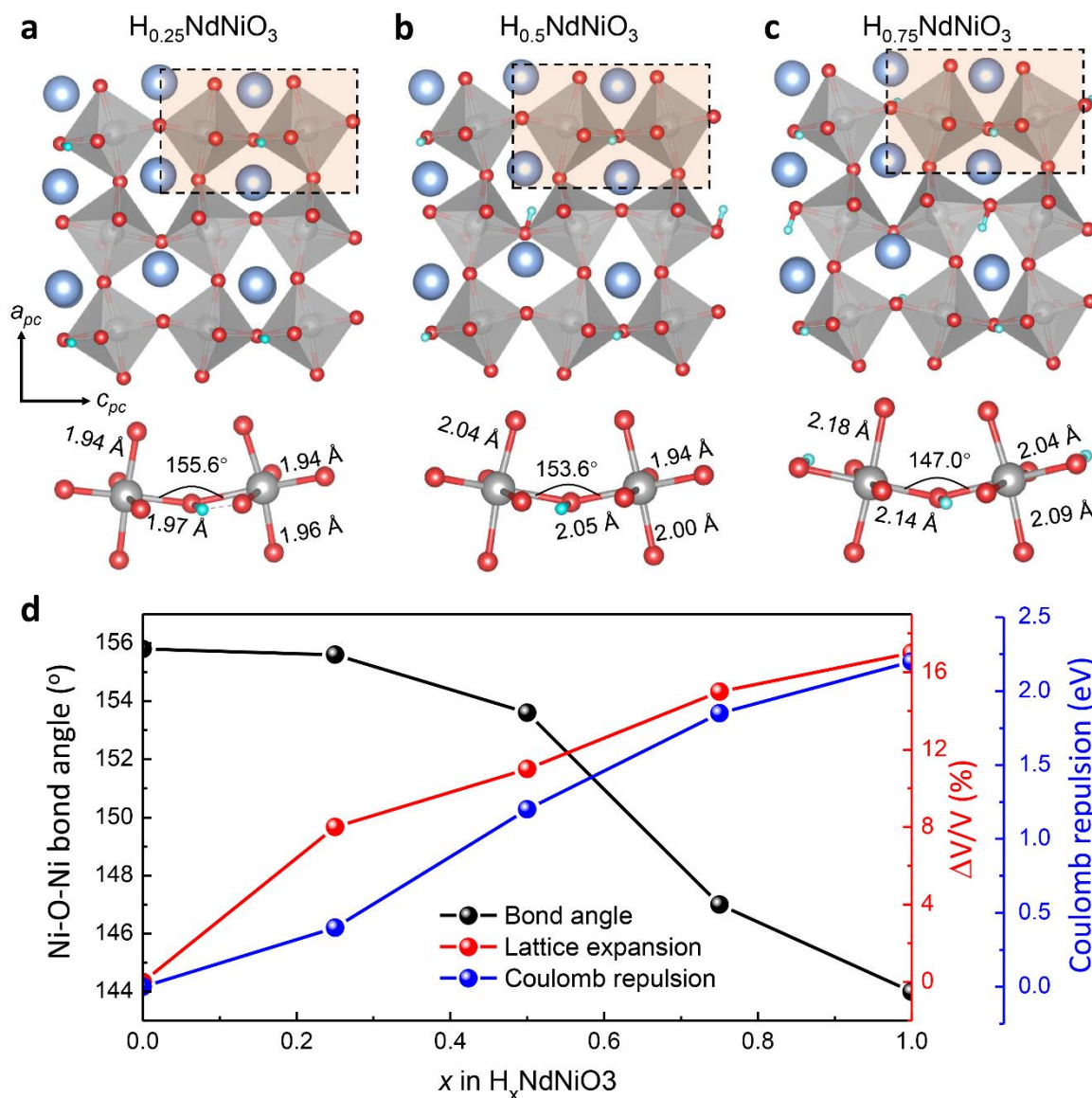
Figure S20. Hydrogen ion concentration dependence of lattice modification and metal-insulator transition. a-c) Calculated lattice distortions of NiO_6 octahedra and Ni-O-Ni bond angle variation for H_xNNO for the different hydrogen concentration. The value of Ni-O-Ni angle (θ) and Ni-O bond lengths (L) are labeled. d) Hydrogen ion concentration dependent Ni-O-Ni bond angle, degree of volume expansion (ΔV) as well as the Coulomb repulsive energy (U), which shows that the bond angles decrease along the hydrogen ion concentration, while the lattice volume and the Coulomb repulsive energy increase with the hydrogen ion intercalation.
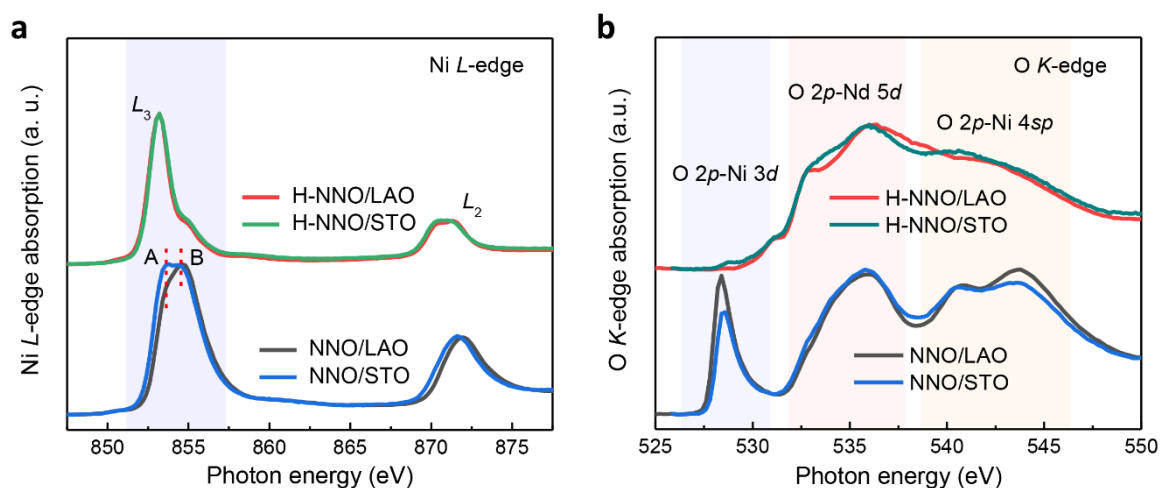
Figure S21. Comparison of X-ray absorption spectra of (a) Ni *L*-edge and (b) O *K*-edge for NNO and H-NNO on STO and LAO substrate, from which we know that nearly the same results can be obtained with the hydrogen ion intercalation induced phase transformations. In the Ni XAS, the feature A represents the d^8-like configuration of Ni in NNO and feature B indicates the ligand hole states around the Fermi level.
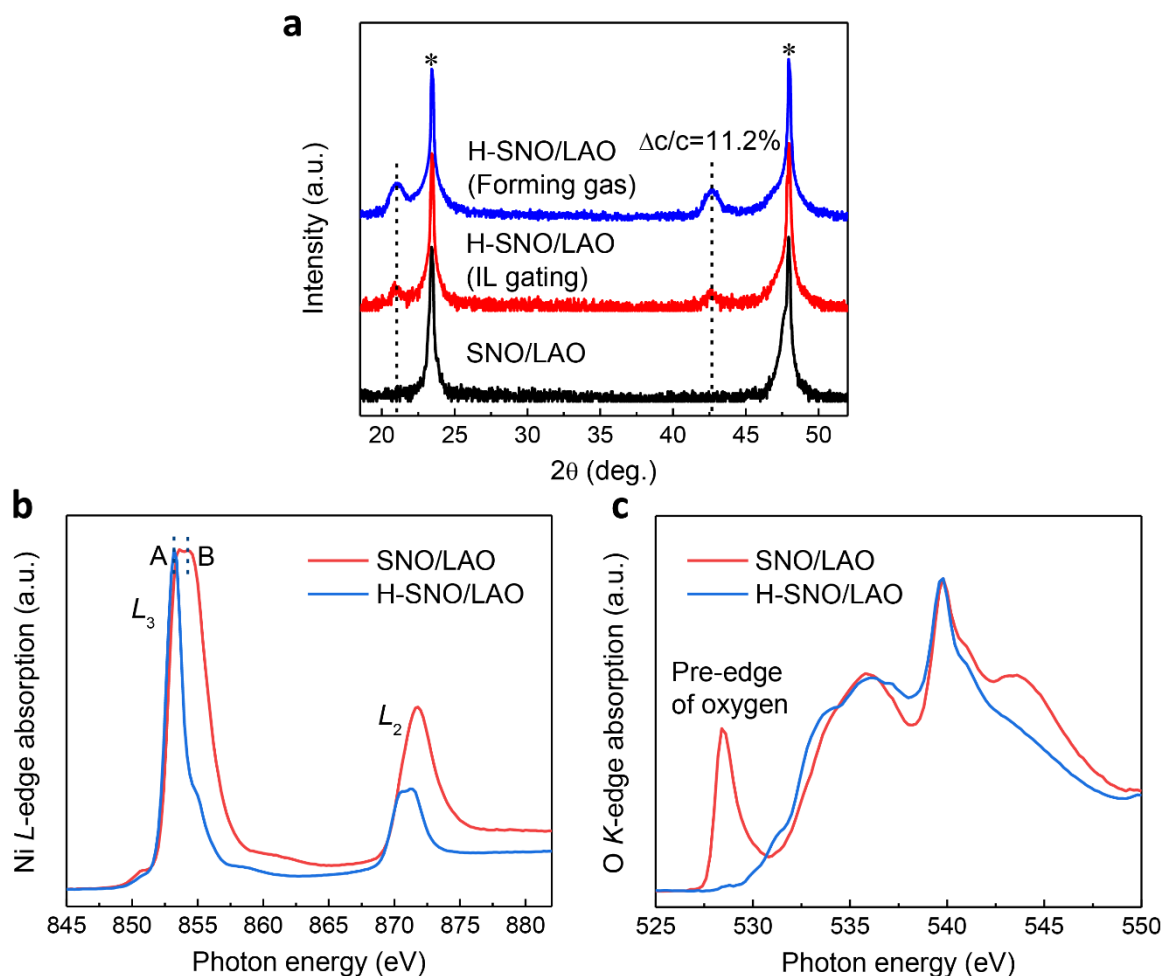
Figure S22. a) Phase transformation of the SmNiO₃ (SNO) from pristine to hydrogen ion intercalated phase with the lattice expansion of 11.2% through ionic liquid gating and Pt catalysis in forming gas. b, c) Corresponding XAS spectra of the Ni L-edge and O K-edge before and after hydrogenation. The features A and B in Ni L-edge represent the d^8-like configuration of Ni in NNO and the ligand hole states around the Fermi level, respectively. For the SmNiO₃, the hydrogenation results show similar change to that of hydrogen ion induced phase transformation in NdNiO₃, in which the feature B in the Ni L-edge and the pre-edge of O K-edge are almost disappeared.
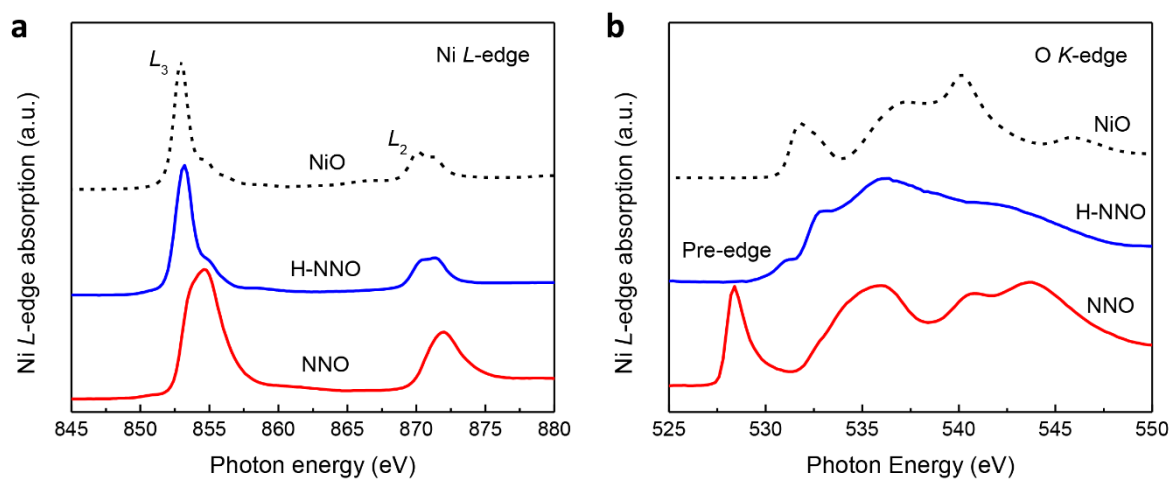
Figure S23. Comparison of (a) Ni *L*-edge and O *K*-edge X-ray absorption spectra among NNO, H-NNO and NiO, from which we know that they show the similar characteristic of the Ni *L*-edge for H-NNO and NiO.
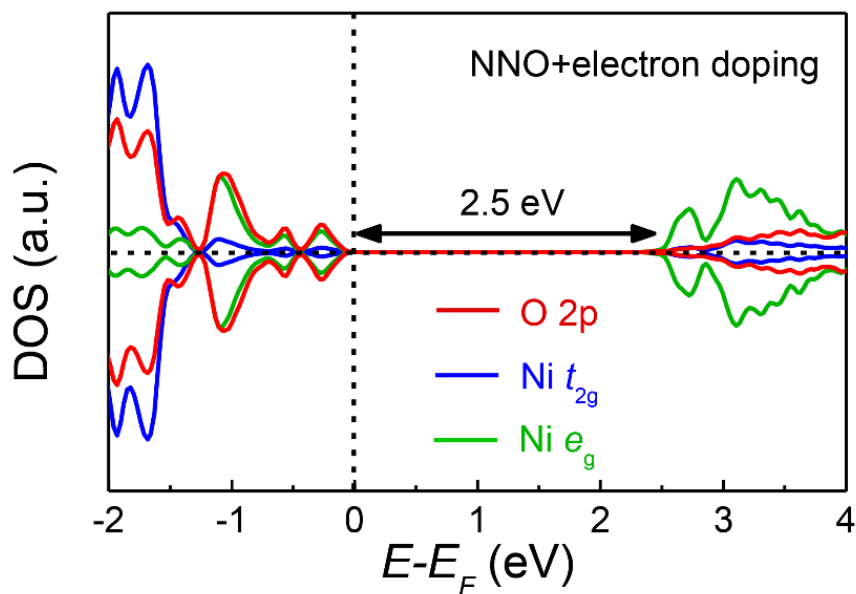
Figure S24. Spin polarized projected density of states (PDOS) of the electron doped NNO (e-NNO) with concentration of 1e/f.u. and the lattice structure same as pristine NNO. Since the empty Ni-O hybridized orbitals are fully filled by excess electrons, the system changes to the insulator with band gap ~2.5 eV.
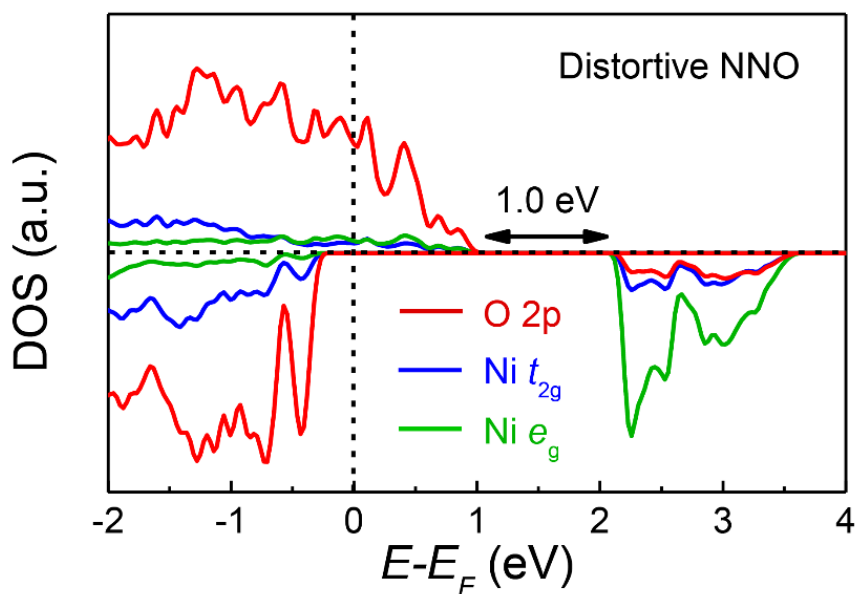
Figure S25. Projected density of states (PDOS) of the lattice distortive NNO. The lattice structure is adopted from the H-NNO but removing all H atoms. The Coulombic repulsion energy is labeled by black arrows.
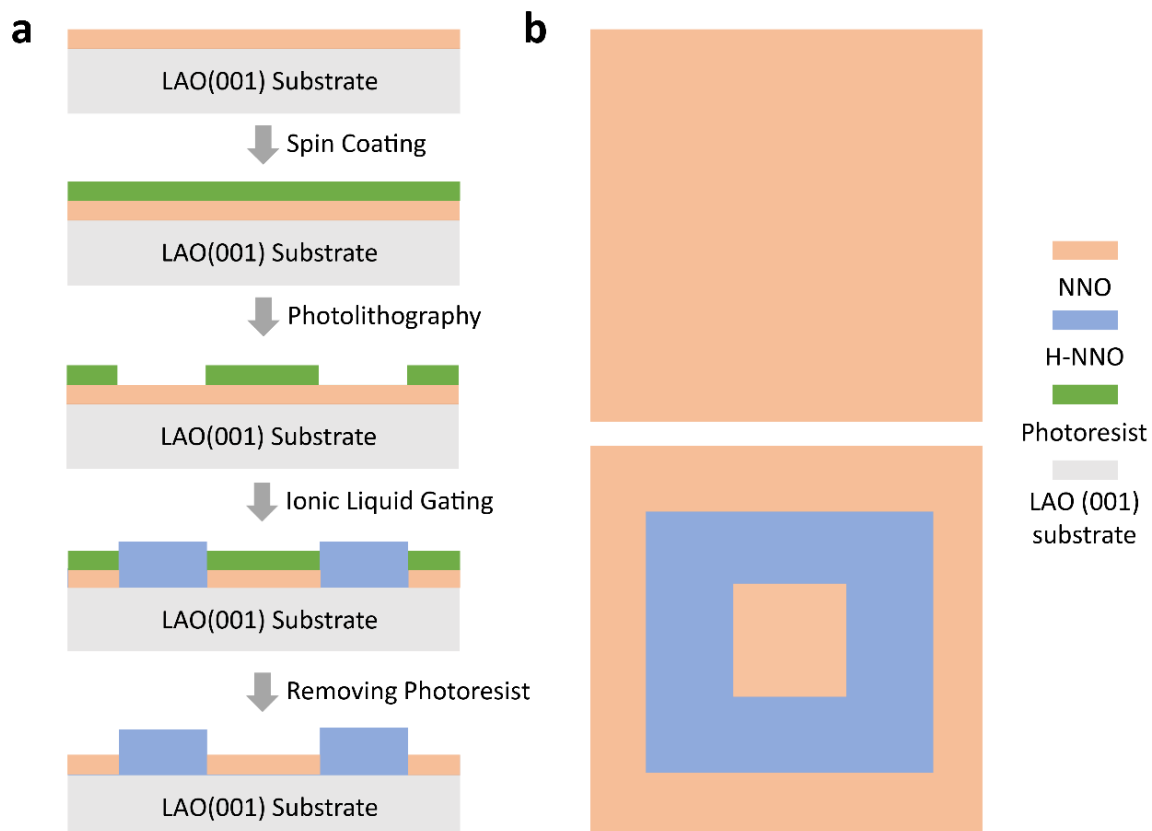
Figure S26. Fabrication process of the micropattern with selective area phase transformation in the ionic liquid gating process for the (a) cross and (b) top views, respectively, from which we see that the lattice expansion and metal-insulator transition can be clearly identified through the synergistic effect between ion and charge in the process of ionic liquid gating.

References

[1] N.P. Lu, P.F. Zhang, Q.H. Zhang, R.M. Qiao, Q. He, H.B. Li, Y.J. Wang, J.W. Guo, D. Zhang, Z. Duan, Z.L. Li, M. Wang, S.Z. Yang, M.Z. Yan, E. Arenholz, S.Y. Zhou, W.L. Yang, L. Gu, C.W. Nan, J. Wu, Y. Tokura, P. Yu, *Nature* **2017**, *546*, 124.

[2] Y. Zhou, X.F. Guan, H. Zhou, K. Ramadoss, S. Adam, H.J. Liu, S. Lee, J. Shi, M. Tsuchiya, D. D. Fong, S. Ramanathan, *Nature* **2016**, *534*, 231.

[3] T.T. Huang, Y.J. Wang, H.B. Li, M. Wang, Y.J. Lyu, S.C. Shen, N.P. Lu, Q. He, P. Yu, *Appl. Phys. Lett.* **2019**, *114*, 221907.

[4] J.N. Reimers, J.R. Dahn, *J. Electrochem. Soc.* **1992**, *139*, 2091.

[5] M. Wang, L. Hao, F. Yin, X. Yang, S.C. Shen, N.L. Zou, H. Cao, J.Y. Yang, N.P. Lu, Y.S. Wu, J.B. Zhang, H. Zhou, J. Li, J. Liu, P. Yu, *Adv. Funct. Mater.* **2021**, *31*, 2100261.

[6] Z.L. Li, S.C. Shen, Z.J. Tian, K. Hwangbo, M. Wang, Y.J. Wang, F. M. Bartram, L.Q. He, Y.J. Lyu, Y.Q. Dong, G. Wan, H.B. Li, N.P. Lu, J.D. Zang, H. Zhou, E. Arenholz, Q. He, L.Y. Yang, W.D. Luo, P. Yu, *Nat. Commun.* **2020**, *11*, 184.

[7] M. Wang, S.C. Shen, J.Y. Ni, N.P. Lu, Z.L. Li, H.B. Li, S.Z. Yang, T.Z. Chen, J.W. Guo, Y.J. Wang, H.J. Xiang, P. Yu, *Adv. Mater.* **2017**, *29*, 1703628.

[8] S.C. Shen, Z.L. Li, Z.J. Tian, W.D. Luo, S. Okamoto, P. Yu, *Phys. Rev. X* **2021**, *11*, 021018.

[9] M. Wang, X.L. Sui, Y.J. Wang, Y.H. Juan, Y.J. Lyu, H.N. Peng, T.T. Huang, S.C. Shen, C.G. Guo, J.B. Zhang, Z.L. Li, H.B. Li, N.P. Lu, A.T. N'Diaye, E. Arenholz, S.Y. Zhou, Q. He, Y.H. Chu, W.H. Duan, P. Yu, *Adv. Mater.* **2019**, *31*, 1900458.

[10] A.K. Padhi, K. S. Nanjundaswamy, J.B. Goodenough, *J. Electrochem. Soc.*, **1997**, *144*, 1188.

[11] S. Chen, Z.W. Wang, H. Ren, Y.L. Chen, W.S. Yan, C.M. Wang, B.W. Li, J. Jiang, C.W. Zou, *Sci. Adv.* **2019**, *5*, eaav6815.

[12] J.C. Hunter, *J. Solid State Chem.* **1981**, *3*, 142.

[13] H.B. Li, F. Lou, Y.J. Wang, Y. Zhang, Q.H. Zhang, D. Wu, Z.L. Li, M. Wang, T.T. Huang, Y.J. Lyu, J.W. Guo, T.Z. Chen, Y. Wu, E. Arenholz, N.P. Lu, N.L. Wang, Q. He, L. Gu, J. Zhu, C.W. Nan, X.Y. Zhong, H.J. Xiang, P. Yu, *Adv. Sci.* **2019**, *6*, 1901432.

[14] J.R. Dahn, R. Fong, M.J. Spoon, *Phys. Rev. B* **1990**, *42*, 6424.

[15] E. Stavitski, F.M.F. de Groot, *Micron* **2010**, *41*, 687.

[16] P.L. Potapov, S.E. Kulkova, D. Schryvers, J. Verbeeck, *Phys. Rev. B* **2001**, *64*, 184110.

[17] B. Mundet, C. Domínguez, J. Fowlie, M. Gibert, J.M, Triscone, D.T.L. Alexander, *Nano Lett.* **2021**, *21*, 2436.